Available online at www.sciencedirect.com

ScienceDirect

Ceramics International 40 (2014) 4975–4984

CERAMICS INTERNATIONAL

www.elsevier.com/locate/ceramint

Chemical and structural analysis related to defects in nanocrystalline $Ba_{1-x}Sr_xTiO_3$ grown via hydrothermal sol–gel

S. Fuentes[a,e,*], F. Céspedes[b], L. Padilla-Campos[c], D.E. Diaz-Droguett[d]

[a]Departamento de Ciencias Farmacéuticas, Facultad de Ciencias, Universidad Católica del Norte, Casilla 1280, Antofagasta, Chile
[b]Departamento de Física, Facultad de Ciencias, Universidad Católica del Norte, Casilla 1280, Antofagasta, Chile
[c]Departamento de Química, Facultad de Ciencias Básicas, Universidad de Antofagasta, Casilla 170, Antofagasta, Chile
[d]Instituto de Física, Facultad de Física, Pontificia Universidad Católica de Chile, Casilla 306, Santiago, Chile
[e]Center for the Development of Nanoscience and Nanotechnology, CEDENNA, Santiago, Chile

Received 27 August 2013; received in revised form 30 September 2013; accepted 30 September 2013
Available online 18 October 2013

Abstract

The chemical and structural properties of $Ba_{1-x}Sr_xTiO_3$ (BST, $x=0$–1) nanoparticles synthesised via sol–gel–hydrothermal were analysed. Two types of salts of Ba ($BaCl_2$ and $Ba(OH)_2$) and Sr ($SrCl_2$ and $Sr(OH)_2$) as starting reactants were used to compare two synthesis methods. Chemical characterisation and oxidation states were obtained using X-ray photoelectron spectroscopy. Structural information was acquired by Raman spectroscopy, and calculations to obtain theoretical Raman spectra associated with the different formed phases of BST were performed for comparison. The results were consistent with the presence of oxygen vacancies in all of the compounds synthesised, but the use of hydroxide salts introduced a minor concentration of oxygen vacancies into the BST compounds. In addition, the presence of oxygen vacancies produced an increase of the intensity of first-order modes of vibration and a minor oxidation state of the Ti atom in the structure. Finally, the oxygen vacancies produced a distortion of the structure, inducing the existence of the non-perovskite phase.

Keywords: B. Defects; B. Spectroscopy; C. Ferroelectric properties; D. $BaTiO_3$; Titanates

1. Introduction

Barium strontium titanate, $Ba_{1-x}Sr_xTiO_3$ or BST, has long been the most extensively studied perovskite ferroelectric oxide. Recently, this material has received significant attention in the electronics industry due to its high dielectric constant, low dielectric loss, good thermal stability and high frequency characteristics [1,2]. Thus, the most promising application of BST is as a candidate for memory storage devices and dynamic random access memories (DRAMs) [3,4].

$Ba_xSr_{1-x}TiO_3$ is a solid solution of $BaTiO_3$ (BT) and $SrTiO_3$ (ST). Partial substitution in the atomic lattice by another isovalent cation (Ba by Sr) modifies both the dielectric and ferroelectric properties of the material [5]. For example, at room temperature, BT and Ba-rich $Ba_xSr_{1-x}TiO_3$ compounds have tetragonal lattices and are ferroelectric, whereas ST and Sr-rich $Ba_xSr_{1-x}TiO_3$ compounds are cubic and paraelectric. Hence, the properties of BST depend on the chemical composition and structural characteristics of its constituent materials. Several methods have been investigated for the preparation of BST in powder form, including the sol–gel method [6], solid-state reactions [7], spray pyrolysis [8], combustion synthesis [9], and microwave [10] and hydrothermal methods [11,12]. The latter method is advantageous due to the low processing temperature, the non-vacuum requirement and the low cost compared to the other methods. The properties of perovskite ferroelectric oxides are highly dependent on the particle size and microstructural characteristics. For example, ferroelectricity decreases with decreasing particle grain size and disappears below a certain critical size [13,14]. Other factors, such as the density, shape, and the presence of

*Corresponding author at: Departamento de Ciencias Farmacéuticas, Facultad de Ciencias, Universidad Católica del Norte, Casilla 1280, Antofagasta, Chile. Tel.: +56 55 2355383; fax: +56 55 2 355632.
E-mail address: sfuentes@ucn.cl (S. Fuentes).

0272-8842/$ - see front matter © 2013 Elsevier Ltd and Techna Group S.r.l. All rights reserved.
http://dx.doi.org/10.1016/j.ceramint.2013.09.134

impurities and structural defects also affect this property [15,16].

The chemical, structural, and morphological characteristics of BST powders grown by the sol–gel–hydrothermal method often vary as a function of the synthesis parameters, such as the reaction time, reaction temperature, and reactant composition. Thus, the study of how these parameters influence the final characteristics of BST is considered significant.

In a previous work we reported the outcome of the reactant type, $BaCl_2$ and $SrCl_2$ or $Ba(OH)_2$ and $Sr(OH)_2$ salts, on the chemical and structural properties of BST nanoparticles grown by the sol–gel–hydrothermal method [17]. The presence of Cl^- ions resulted in a better Sr incorporation into the network of BST when the BA:Sr mole ratio used in the starting reactants was less than one. On the other hand, the presence of OH^- ions led to BST nanoparticles with fewer structural defects, specifically fewer oxygen vacancies. The result of these vacancies was not clearly established but is important because the defects directly influence the final properties of the BST.

The goal of the present study is to compare two synthesis methods, one based on Cl^- ions and the other based in OH^- ions, with respect to the creation of oxygen vacancies. Specifically, we wanted to study the effects of the presence of these defects on the chemical and structural properties of $Ba_{1-x}Sr_xTiO_3$ ($x=0$–1) nanoparticles prepared by the sol–gel–hydrothermal method. To achieve this goal, analysis using X-ray photoelectron spectroscopy (XPS) and Raman spectroscopy (RS) is executed. RS is very sensitive to the deformation of the microstructure and the presence of defects in the material. On the other hand, XPS gives information on the surface chemistry and oxidation states present in the compound. In addition, these studies are complemented with the determination of theoretical Raman spectra from quantum chemical calculations for the different formed phases.

2. Experiments

2.1. Synthesis

$Ba_{1-x}Sr_xTiO_3$ powders prepared using different Ba:Sr mole ratios ($x=0$, 0.3, 0.5, 0.8 and 1) were synthesised using a sol–gel–hydrothermal method. The synthesis involved tetrachloride titanate ($TiCl_4$, 1 M) and two different salts of barium and strontium, $BaCl_2$ and $SrCl_2$ or $Sr(OH)_2$ and $Ba(OH)_2$, as the starting materials.

In method 1 (M1), a typical synthesis of sample (B2) used $BaCl_2{\bullet}2H_2O$ (99.999%, Aldrich) and $SrCl_2{\bullet}6H_2O$ (99.995%, Aldrich) as reactants (Table 1). A solution (A) of 1.1 mL $TiCl_4$ (1 M, Aldrich) was diluted in 2.3 mL of 2 M HCl to form an yellowish solution. The aqueous solution (B) was prepared by dissolving 0.52 g $BaCl_2{\bullet}2H_2O$ and 0.4 g of $SrCl_2{\bullet}2H_2O$ in 20 mL of deionised water. For preparing $BaSrTiO_3$ precursor, solution (B) was added into solution (A) with stirring vigorously for 1 h. Under stirring and N_2 bubbling, 13 mL of 6 M NaOH was added to the barium strontium titanium solution and a white homogeneous colloidal slurry (barium strontium titanium) was formed.

Table 1
The preparing parameters of BST powders synthesised at 180 °C and 24 h.

Samples method 1 (Ml)	Ba:Sr in reactant	Samples method 2 (M2)	Ba:Sr in reactant
B1	1:0	**S1**	1:0
B2	0.7:0.3	**S2**	0.7:0.3
B3	0.5:0.5	**S3**	0.5:0.5
B4	0.2:0.8	**S4**	0.2:0.8
B5	0:1	**S5**	0:1

The mixed solution was transferred into a 100 mL Teflon-lined stainless steel reactor, sealed, and then heated for 24 h at 180 °C under partial oxygen pressure of 60 psi. At the end of the reaction, the autoclave was naturally cooled to room temperature. The as-formed white solid powder that was attached to the bottom and inner wall of the Teflon container was collected, centrifuged, washed with distilled water and ethanol to remove the remaining ions, and dried at 60 °C for 6 h in vacuum [17].

In method 2 (M2), similarly, $Ba_{1-x}Sr_xTiO_3$ powders with $x=0$, 0.3, 0.5, 0.8 and 1 were prepared using $Ba(OH)_2$ and $Sr(OH)_2$ as starting materials (Table 1).

2.2. Characterisation

The surface chemical information of the BST samples was obtained by X-ray photoelectron spectroscopy (XPS; Physical Electronics system model 1257) using an Al K_α emission source. The binding energies and oxidation states were obtained from high-resolution scans. The energy scale was calibrated by assigning 284.8 eV to the C 1s peak, corresponding to adventitious carbon. The Raman spectra were recorded on a WITEC model CRC200 using a 5.5 mW laser with a wavelength of 514.5 nm.

3. Theoretical study

The theoretical calculations were performed using the B3LYP exchange correlation functional [18–21], the same that was used in a previous study [17]. For the titanium and oxygen atoms, the 6–31 G basis set [22] was used. For the barium and strontium atoms, the pseudopotential of the Los Alamos group [23] with a corresponding basis set was used. Crystallographic data were used to represent the initial cubic phases for BT, ST and BST reported in the literature [24–26]. The vibrational frequencies and Raman intensities were calculated by setting the second derivatives of the energy with respect to the Cartesian nuclear coordinates and transforming to mass-weighted coordinates. Population analysis based on atomic polar tensors (APT) was utilised for discussion of the results [27]. All computations were performed using the Gaussian 09 programme [28].

4. Results

4.1. Raman spectroscopy

Tetragonal BT single crystals at room temperature (space group: *P*4*mm*) have atomic displacements that exhibit ferroelectricity. In the interval of 120–1460 °C, BT monocrystals take the paraelectric cubic perovskite structure (space group *Pm*3*m*). The vibrational modes in the cubic structure are $3F1u+F2u$ [29]. Each of the *Fu* modes is triply degenerate, and all of them are of odd symmetry with respect to the inversion. Therefore, RS became inactive. The lowered unit cell symmetry of the tetragonal BT caused each of the three *F*1*u* modes to split into A1+E and the *F*2*u* mode to split into B1+E. The symmetric *A*1 and *E* modes were Raman active. Therefore, the tetragonal phase can be distinguished by displaying Raman active modes in vibrational spectroscopy.

In contrast to BT, ST single crystals at room temperature have an ideal cubic perovskite structure (space group: *Pm*3*m*). Because all the zone-centre optical phonons are of odd symmetry, no first-order Raman activity is expected based on the factor group symmetry analysis; instead, the room temperature spectrum should be dominated by second-order scattering [30]. However, studies of the Raman spectra of ST have shown that first-order Raman scattering is observed. This occurs when the central symmetry is broken due to many factors, such as strain effects, the presence of impurities or oxygen vacancies, and even external conditions [31–33].

Fig. 1a and b shows the Raman spectra of BT (B1 and S1) and ST (B5 and S5), respectively, synthesised by two methods, M1 and M2. Fig. 1a reveals that for both methods, there are five phonon line characteristics: the broad bands at approximately 180 cm^{-1} [A1(TO), E(LO)] and 265 cm^{-1} [A1(TO)], sharp bands at approximately 307 cm^{-1} [B1, E(TO+LO)] 520 cm^{-1} [A1, E(TO)], and 720 cm^{-1} [A1, E(LO)] are the characteristic peak active modes of the tetragonal phase of BT [23]. *Chávez* et al. [26] reported that a slight distortion in the structure of the cubic BT phase led to the appearance of the characteristic peaks for a tetragonal phase in the Raman spectrum, which indicates a transition from the cubic to the pseudotetragonal phase.

In Fig. 1b (iv), for sample B5, there are five photon lines at approximately 180, 340, 479, 540, and 796 cm^{-1} that are ascribed to TO_2, TO_3, LO_2, TO_4 and LO_4 first-order modes, respectively. The TO_2 and TO_4 phonons are associated with O–Ti–O bonding. The intensities of the bands ascribed to the second-order modes present much weaker intensity compared with the first-order bands [34]. In the S5 sample, five broad Raman bands are observed at 247 (TO_1+TA), 301 [(TO_2+TA); (TO_2+TO_1); (TO_4-TO_2)], 391 [(TO_4+TA); (TO_4+TO_2)], 635 ($2TO_3$) and 726 cm^{-1} (TO_4+TO_2). The intensities of the bands are ascribed mainly to the second-order modes, consistent with the reported data [30] and are shown by (*) in curve (iii). In this case, the intensities of the bands ascribed to the first-order modes present much weaker intensity compared to the first-order peaks (TO_2, TO_4 and LO_4) shown in curve (iv) [34].

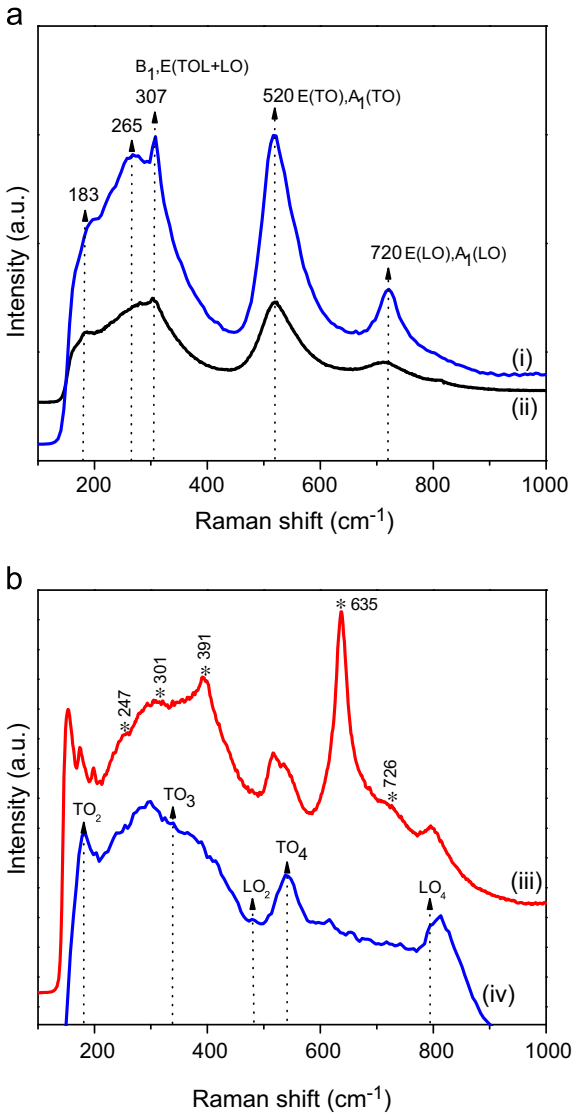

Fig. 1. Raman spectra of $BaTiO_3$ and $SrTiO_3$ samples synthesised by two methods M1 and M2: (i) S1, (ii) B1, (iii) S5 and (iv) B5.

The Raman spectra of the $Ba_{1-x}Sr_xTiO_3$ powders with $x=0.3$, 0.5 and 0.8 (BST) prepared by both methods are shown in Fig. 2. In general, a broadband structure was identified, which corresponds to a background for the "single-phonon" bands due to the existence of a relaxation process [35].

For the concentration of Sr to $x=0.3$, the characteristic bands of the BT structure located at ≈188, 265, 307, 520 and 720 cm^{-1} in both methods are decreased (bands identified by ♦ in B2 and S2). The decrease is more significant for the sample grown under M1, and, in both methods, the sample exhibits broad Raman bands associated with the presence of Sr (Fig. 2a).

With the increased Sr to $x=0.5$ in the samples B3 and S3, the appearance of first-order Raman bands at ≈185 (TO_2), 340 (TO_3), 538 (TO_4) and 791 (LO_4) cm^{-1} and 182 (TO_2), 342 (TO_3), 488 (LO_2) and 540 (TO_4) cm^{-1} are observed, indicating a lower crystal symmetry induced mainly by

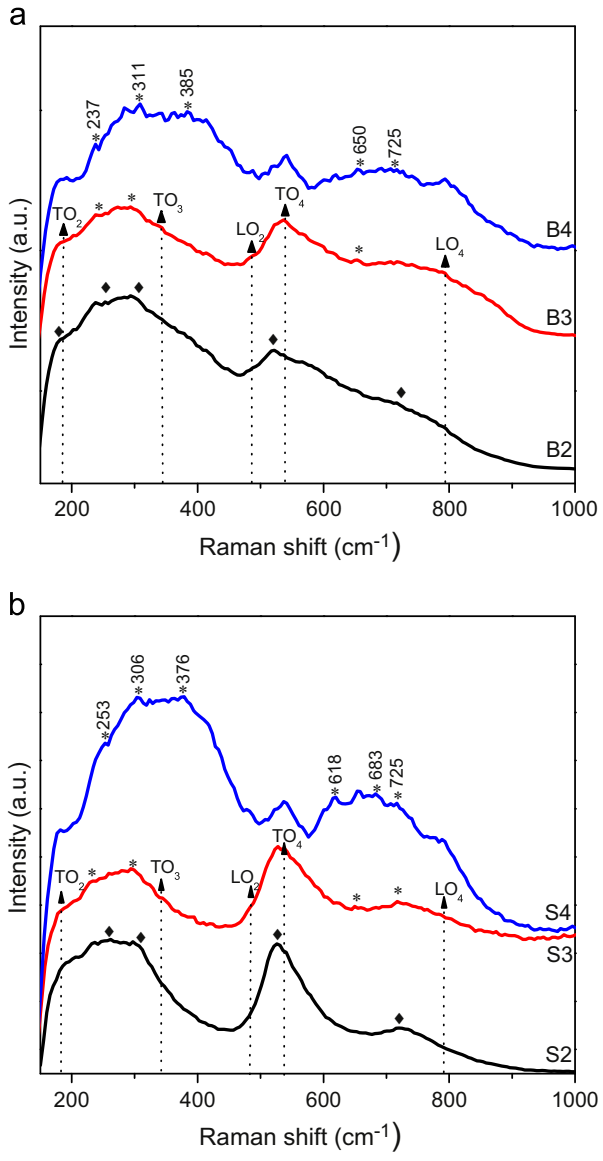

Fig. 2. Raman spectra of $Ba_xSr_{1-x}TiO_3$ samples with $x=0.3$, 0.5 and 0.8 synthesised by two methods: (a) M1 and (b) M2.

defects. The Raman selection rule was relaxed in comparison with the ST bulk [34]. On the other hand, three broad Raman bands are observed at 238, 294, and 650 cm^{-1} in B3, and five broad Raman bands are observed at $\approx$248, 260, 296, 650, and 720 cm^{-1} in S3. These bands are assigned to the second-order modes, consistent with the effects reported in reference [34].

When the concentration of Sr is increased to $x=0.8$ in samples B4 and S4, the first-order Raman bands described above maintain their intensity (TO_2, LO_2, TO_4 and LO_4), whereas the intensity for most of the second-order modes characteristic of Sr show a gradual increase.

The frequencies of the observed phonon bands of the BT (B1 and S1), ST (B5 and S5) and BST samples grown by the two methods, M1 and M2, are given in Table 2. The following phonon modes are present in the spectra of the BST powders for all Sr concentrations studied: the TO_2, LO_2, TO_3, TO_4, and LO_4 modes, respectively. However, the TO_1 soft mode (A_1 and E components) was not distinguished at room temperature in all compositions of the samples grown under the two methods [36,37].

4.2. X-ray photoelectron spectroscopy

The XPS results from the BST samples prepared by both methods (M1 and M2) are summarised in Table 3. The values of the binding energy (BE) for the Ba 3d doublet of the samples prepared under M1 (B2 to B4) correspond to Ba atoms in a non-perovskite structure of BST, also called the decomposed perovskite structure or the β-component of Ba [38]. On the contrary, the BE values for the Ba 3d signal of samples S2 and S3 prepared under M2 are closer to the values reported for Ba atoms in the perovskite structure of BST, also called the α-component of Ba [39,40]. Only the values of the Ba 3d doublet from the sample S4 correspond to the β-component of Ba. On the other hand, the BE values for the Sr 3d doublet for all samples are attributed to Sr atoms in the perovskite structure of BST or the α-component of Sr. The reported BE values for the Sr atoms in the non-perovskite

Table 2
Frequencies (cm^{-1}) of observed lines in the Raman spectra of BST samples prepared by M1 and M2.

$BaTiO_3$ B1 and S1	$SrTiO_3$ B5 1er order	$SrTiO_3$ S5 2nd order	$Ba_{1-x}Sr_xTiO_3$ $X=0.3$		$Ba_{1-x}Sr_xTiO_3$ $X=0.5$		$Ba_{1-x}Sr_xTiO_3$ $X=0.8$	
			B2	S2	B3	S3	B4	S4
180(A_1(TO),E(LO))	180 (TO_2)	247(TO_1+TA)	181	182	185	182	185	182
265 (A_1(TO))	340 (TO_3)	301(TO_2+TA);	236	234	237	230	237	253
307(B1,E(TO+LO))	479 (LO_2)	(TO_2+TO_1);	294	260	294	260	311	306
520(A_1,E(TO))	540 (TO_4)	(TO_4−TO_2)	520	295	541	295	340	376
720(A_1,E(LO))	796 (LO_4)	391(TO_4+TA);	720	526	650	342	385	539
		(TO_4+TO_2)		724	790	527	541	618
		635 ($2TO_3$)				650	620	655
		726(TO_4+TO_2)				720	650	683
							725	725
							794	790

Table 3
Binding energies data in electron volt of the BST samples prepared by M1 and M2.

Sample	Ba		Sr		Ti^{4+}		Ti^{3+}		O	
	$3d_{5/2}$	$3d_{3/2}$	$3d_{5/2}$	$3d_{3/2}$	2p3/2	2p1/2	2p3/2	2p1/2	O^{-2}	O^{x-}
B2	780.4	795.7	133.4	135.2	458.8	464.6	457.0	462.8	530.4	532.4
B3	780.0	795.3	132.6	134.4	458.3	464.1	457.2	462.9	529.8	531.6
B4	780.5	795.8	133.4	135.2	458.7	464.5	457.0	462.7	530.4	532.3
S2	779.5	794.8	132.6	134.4	458.2	464.0	456.8	462.6	529.7	531.6
S3	779.6	794.8	132.6	134.4	458.2	463.9	457.0	462.6	529.6	531.3
S4	780.0	795.3	132.7	134.5	458.4	464.1	456.7	462.3	529.9	531.6

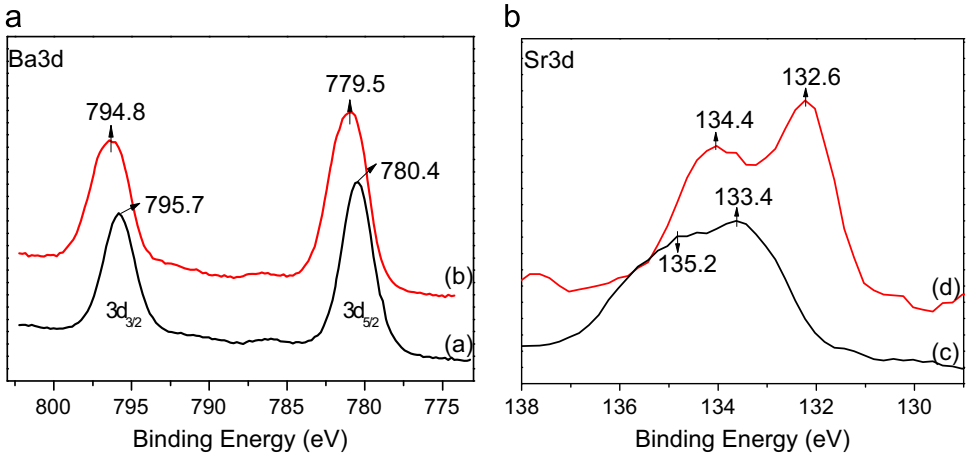

Fig. 3. XPS spectra from the Ba 3d and Sr 3d signals for samples B2 (a, c) and S2 (b, d).

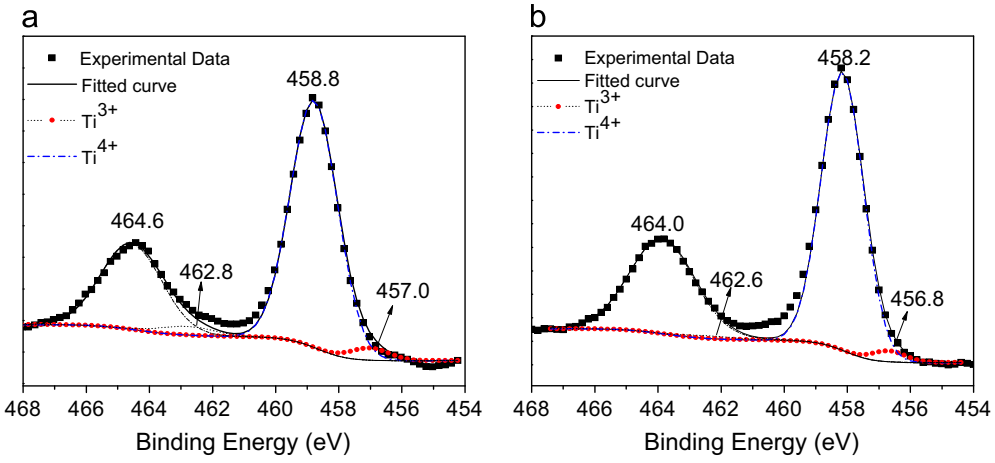

Fig. 4. XPS spectra of the Ti 2p signal for the samples B2 and S2: (a) M1 and (b) M2.

structure (β-component of Sr) have higher values, above 133.7 and 135.5 eV for Sr $3d_{5/2}$ and Sr $3d_{3/2}$, respectively [39–41], values that in our synthesised BST were not found. The XPS spectra from the Ba 3d and Sr 3d signals for the samples B2 and S2 prepared using the same Ba:Sr mole ratio in the reactants are depicted in Fig. 3. A more-defined Sr 3d doublet is revealed in sample S2.

Curve fitting was performed on the Ti 2p and O 1s signals because changes in the oxygen oxidation states are strongly associated with Ti oxidation state changes. The Ti 2p signal acquired from all samples (B2 to S4) was fitted using two curves associated with Ti with oxidation states +4 and +3. A typical fit performed on the spectra is shown in Fig. 4, where fits for the Ti 2p signal from samples B2 and S2 are depicted.

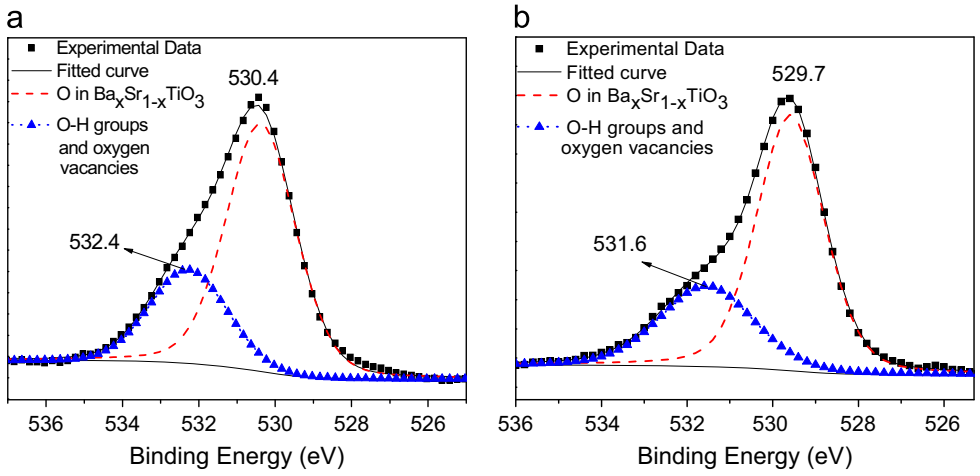

Fig. 5. XPS spectra of the O 1s signal for the samples B2 and S2: (a) M1 and (b) M2.

The BEs of the stronger peaks correspond to Ti^{4+} ions related to Ti in the perovskite structure of BST (α-Ti) [39,40]. The BEs of the weak peaks were attributed to Ti^{3+} ions. These ions correspond to a Ti_2O_3 compound, which is related to the non-perovskite structure of BST [39,40]. The BE values for Ti^{3+} and Ti^{4+} ions from all the BST samples are summarised in Table 3. Peaks attributed to Ti^{2+} ions related to TiO were not detected in the spectra.

The O 1s signal acquired from all samples (B2–S4) was also fitted using two curves. A typical fit of the O 1s spectra is shown in Fig. 5, where the fit results for samples B2 and S2 are depicted. The stronger peak is associated to O^{2-} ions related to oxygen in the perovskite structure of BST, indicating that the oxygen ions remain coordinated in TiO_6 octahedra [41]. The weak peak is attributed to an intermediate oxidation state of oxygen, O^{x-} $(0 < x < 2)$, and it may be related to the hydroxyl (OH) groups, as well as to defects such as oxygen vacancies present in the BST structure. The oxidation state O^{x-} is ascribed to oxygen in the non-perovskite structure of BST [42]. This variation of the oxidation state of oxygen is accompanied by that of Ti, which revealed presence of Ti^{3+} ions, as shown in Fig. 4. If Ti^{4+} ions are located near oxygen vacancies, they can capture one electron and change to Ti^{3+} [41]. The BE values of the peaks associated to the O^{2-} ions and OH groups plus oxygen vacancies (O^{x-} state) are indicated in Table 3. The presence of this O^{x-} state $(0 < x < 2)$ by XPS in all BST samples is consistent with the Raman results acquired from the same set of samples, where effectively first-order Raman peaks attributed to the defects of oxygen vacancies were detected, especially in the samples with compositions of $x \geq 0.5$.

The effect of the preparation method (M1 and M2) on the oxygen percentage in the oxidation states of O^{2-} and O^{x-} found in the BST samples is displayed in Fig. 6. This oxygen percentage was estimated using the value of the area under the curve (peak area) of the peaks associated with the oxidation states O^{2-} and O^{x-} (see Fig. 5) from the O 1s spectrum acquired for each BST sample. Fig. 6 divulges that the samples prepared with a Ba:Sr mole ratio in the reactants of 0.7:0.3, samples B2 and S2, have a similar percentage of oxygen associated with O^{x-}, approximately 29% (and 71% of oxygen associated with O^{2-}). However, the samples prepared with Ba:Sr mole ratios of 0.5:0.5 and 0.2:0.8, samples B3 and S3 and B4 and S4, respectively, revealed a significant difference of the O^{x-} percentage found in the BST compound. For these samples, the presence of oxygen in state O^{x-} is greater under M1 method than M2, with differences exceeding 5%, indicating, that the M1 method would induce more defects and the presence of chemisorbed species in the synthesised BST. Finally, it is important to highlight that the O^{x-} percentages (or inversely, the O^{2-} percentages) from the samples prepared under M1 are very similar independently of the Ba:Sr mole ratio in the reactants used in the preparation, as revealed in Fig. 6.

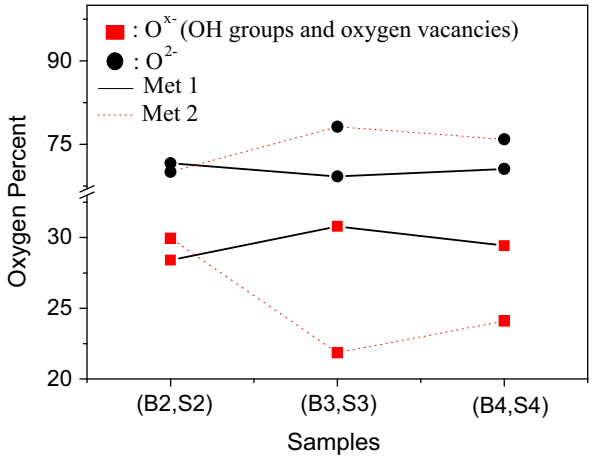

Fig. 6. Percentage of O^{2-} and O^{x-} in BST samples prepared by M1 and M2.

4.3. Theoretical calculations

To give better support to the experimental results with regard to the formed phase of $Ba_{1-x}Sr_xTiO_3$, we proceeded to perform quantum chemical calculations to obtain the

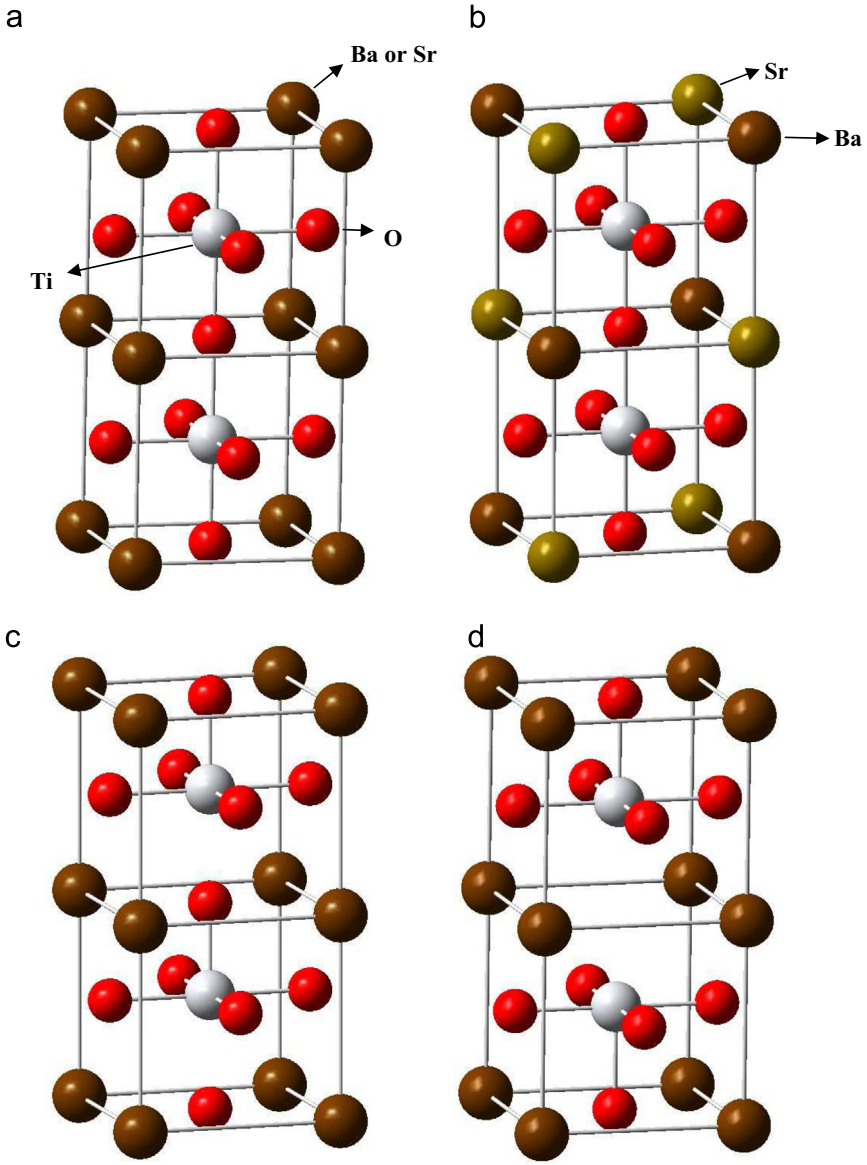

Fig. 7. Cluster model structures. (a) cubic, (b) cubic BST, (c) tetragonal distortion and (d) oxygen vacancy.

theoretical Raman spectra for the compounds with compositions of $x=0$, 0.5, and 1. The electronic and spectroscopic properties were computed by solving the Kohn–Sham equations into an atomic basis set formed by Gaussian functions in a standardised form, as was calculated in a previous study [17].

To simulate the different solid compounds, the cluster methodology [43–45] was used, i.e., a finite number of atoms were used to symbolise the different stages. Fig. 7 shows the cluster models, which represent (a) the initial cubic structure of perovskite type, (b) cubic BST showing the distribution of Ba and Sr in the structure, (c) the distorted cubic structure of tetragonal type, shifting the TiO_4 plane along the Z-axis by 0.1 Å, and (d) structure by oxygen vacancy, for compositions of $x=0$, 0.5 and 1. For each of these structures, the simulated Raman spectra are shown in Fig. 8. The following results were found. First, deformation of TiO_4 plane produces new vibrational frequencies associated with the Ti–O deformation without significantly changing the intensities of the referential frequencies of vibration, the cubic structure of the perovskite type, associated to the theoretical prediction of second-order modes, Fig. 8(i) in all compounds (BT, ST and BST), as can be seen in Fig. 8(ii). These new vibrational frequencies are associated with the first-order modes. Second, the oxygen vacancy produces drastic changes in the vibrational intensities with the appearance of intense new vibrational frequencies also associated with Ti–O deformation in all compounds. The main new frequencies appear at 165, 340, and 478 cm^{-1} for ST, 201, 354, and 454 cm^{-1} for BST and 200, 378, and 405 cm^{-1} for BT. Due to the high intensity of the new frequencies, approximately six times greater in relation to the main frequencies, these new frequencies disguise those related to the second-order modes of cubic structures.

From a previous study [17] we established that the deformation originated for the shifting of the TiO_4 plane or

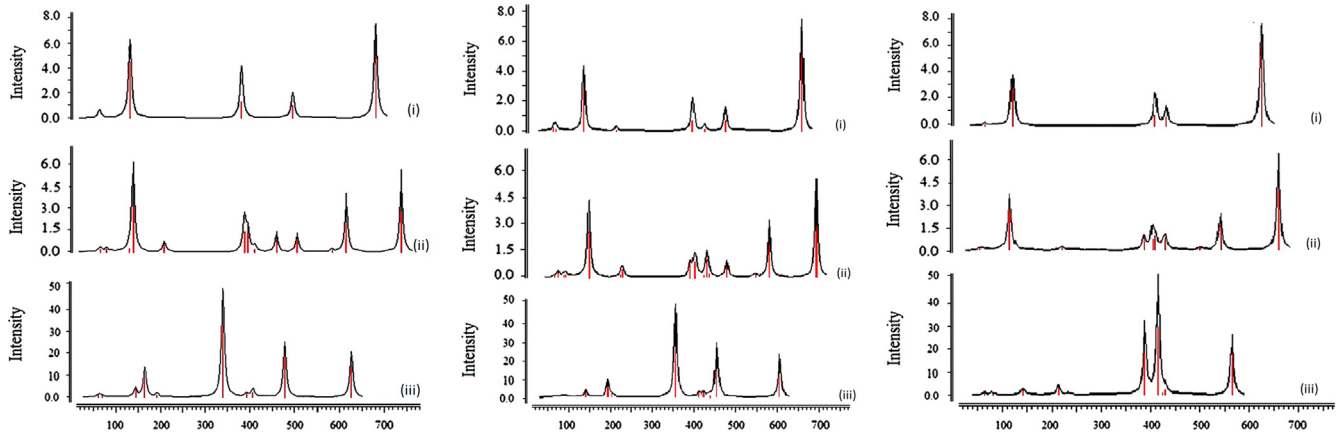

Fig. 8. Theoretical Raman spectra: (a) ST, (b) BST ($x=0.5$) and (c) BT, where, (i) without distortion, (ii) tetragonal distortion and (iii) oxygen vacancy.

tetragonal type did not significantly change the oxidation state of the Ti atom. The oxygen vacancy produces a decrease of the oxidation state of the Ti atom of almost one unit, i.e., $|\Delta Q| \approx 1$ with "Q" the net charge, showing the possible existence of Ti^{+3} in the structure, a result that is in agreement with our XPS results.

5. Summary and discussion

1) The Raman results show that the tetragonal phase is formed for BT. Nevertheless, the spectra are better resolved from samples synthesised from M2 than from M1. That is, in M2, the characteristic peaks of the tetragonal phase present the highest intensity in comparison to the M1. In addition, the peak at 307 cm^{-1} is less defined in M1, the peak that was established as characteristic of the presence of the tetragonal phase [26]. Low intensity and loss of the peak at 307 cm^{-1} is indicative of the dominance of the cubic phase, the presence of impurities or the deformation of the microstructure [26].
2) The Raman results show also the dominance of the second-order modes for ST synthesised under M2. On the other hand, M1 shows dominance for the first-order Raman modes for the same compound. Theoretical calculations showed that the dominance of the first-order modes was induced mainly by the oxygen vacancies, producing a masking of the second-order modes. Consequently, the M2 produces nanoparticles of ST with fewer defects in the microstructure.
3) The Raman results show the existence of first order modes for BST compounds, which are in general high in intensity in comparison with the second order modes. According to *Nilsen et al.*, the appearance of first-order Raman bands at $\approx$180, 540 and 790 cm^{-1} in BST compounds indicates a lower crystal symmetry induced by impurities and defects as oxygen vacancies, very common in perovskites, and suggests a non-centrosymmetric occupation of the Ti atom in the TiO_6 octahedra [34]. The decreased symmetry may also be associated with the frozen dipole moments. This polarisation penetrates into the crystal, giving a local tetragonal structure and destroying the inversion symmetry [36].
4) The XPS results show the existence of an O^{x-} $(0<x<2)$ oxidation state in all samples associated with chemisorbed species and the presence of oxygen vacancies. These results are suggestive of a loss of symmetry with respect to a perovskite structure, causing the first-order modes in the Raman spectra. However, the major presence of oxygen in the O^{x-} state was detected in the samples prepared under M1.
5) The theoretical calculations show that oxygen vacancies produce high intensities of new bands attributed to first order modes, which mask the second order modes. In addition, oxygen vacancies induce a decrease of the oxidation state of the Ti atoms, which a pure tetragonal distortion does not [17].

6. Concluding remarks

$Ba_{1-x}Sr_xTiO_3$ compounds with different compositions and synthesised using two methods were examined. The analysis of the structure of the compounds using Raman and supported by the theoretical calculations was consistent with the presence of oxygen vacancies in all compounds synthesised. A high percentage of oxygen vacancies results in an increase of the intensity of the first-order modes of vibration and a minor oxidation state of the Ti atom in the structure. In addition, the oxygen vacancies can produce a distortion of the structure by shifting the Ti or O atoms, which induces the existence of the non-perovskite phase. Lastly, we conclude from the standpoint of the compound synthesis that M2 produces less oxygen vacancies and therefore, a minor deformation of the compound lattice.

Acknowlegments

This work has been partially financed by FONDECYT grant under Contract no. 1110555. Basal Financing Programme CONICYT, FB0807 (CEDENNA). Proyectos de la Dirección de Investigación (U. de Antofagasta), Grand DI-CODEI-2010-01. The authors thank Professor Victor Fuenzalida from Physics

Department of Universidad de Chile for the use of XPS instrument.

References

[1] S. Ezhilvalavan, T. Tseng, Progress in the developments of (Ba,Sr)TiO_3 (BST) thin films for Gigabit era DRAMs, Mater. Chem. Phys. 65 (2000) 227–248.

[2] J. Wang, T. Zhang, R. Pan, J. Jiang, Z. Ma, C. Xiang, Investigation on the dielectric properties of (Ba,Sr)TiO_3 thin films on hybrid electrodes, Mater. Chem. Phys. 121 (2010) 28–31.

[3] A. Ioachim, M. Toacsan, M. Banciu, L. Nedelcu, F. Vasiliu, H. Alexandru, C. Berbecaru, G. Stoica, Barium strontium titanate-based perovskite materials for microwave applications, Prog. Solid State Chem. 35 (2007) 513–520.

[4] J. Jeon, Effect of $SrTiO_3$ concentration and sintering temperature on microstructure and dielectric constant of $Ba_{1-x}Sr_xTiO_3$, J. Eur. Ceram. Soc. 24 (2004) 1045–1048.

[5] N.C. pramanik, N. Anisha, P.A. Abraham, N. Rani Panicker, Preparation of $Ba_xSr_{1-x}TiO_3$ (x=0–1) nanoparticles by wet-chemical decomposition of Ti-complex and study their dielectric properties, J. Alloys Compd. 476 (2009) 524–528.

[6] X. Shun Hua, J. Wei Fen, L. Kun, X. Jin Hong, Z. Lin, Structure and ferroelectric properties of barium titanate films synthesised by sol–gel method, Mater. Chem. Phys. 127 (2011) 420–425.

[7] J. Li, D. Jin, L. Zhou, J. Cheng, Dielectric properties of barium strontium titanate (BST) ceramics synthesised by using mixed-phase powders calcined at varied temperatures, Mater. Lett. 76 (2012) 100–102.

[8] D.S. Jung, S.K. Hong, J.S. Cho, Y.C. Kang, Morphologies and crystal structures of nano-sized $Ba_{1-x}Sr_xTiO_3$ primary particles prepared by flame spray pyrolysis, Mater. Res. Bull. 43 (2008) 1789–1799.

[9] J. Barrel, K. MacKenzie, E. Stytsenko, M. Viviani, Development of pyroelectric-ceramics for high-temperature applications, Mater. Sci. Eng. 161 (2009) 125–129.

[10] A.Z. Simões, F. Moura, T.B. Onofre, M.A. Ramirez, J.A. Varela, E. Longo, Microwave-hydrothermal synthesis of barium strontium titanate nanoparticles, J. Alloys Compd. 508 (2010) 620–624.

[11] W. Xiao, X. Gang, R. Zhaohui, W. Yonggang, S. Ge, H. Gaorong, Composition and shape control of single-crystalline $Ba_{1-x}Sr_xTiO_3$ (x=0–1) nanocrystals via a solvothermal route, J. Cryst. Growth 310 (2008) 4132–4137.

[12] H. Avila, L. Ramajo, M. Reboredo, M. Castro, R. Parra, Hydrothermal synthesis of $BaTiO_3$from different Ti-precursors and microstructural and electrical properties of sintered samples with submicrometric grain size, Ceram. Int. 37 (2011) 2383–2390.

[13] T. Hoshina, S. Wada, Y. Kuroiwa, T. Tsurumi, Composite structure and size effect of barium titanate nanoparticles, Appl. Phys. Lett. 93 (2008) 192914–192917.

[14] A. Sundaresan, R. Bhargavi, N. Rangarajan, U. Siddesh, C.N. Rao, Ferromagnetism as a universal feature of nanoparticles of the otherwise nonmagnetic oxides, Phys. Rev. B 74 (2006) 161306–161310.

[15] R. Zhang, J. Li, D. Viehland, Self-assembly of point defects into clusters and defectfree regions: a simulation study of higher-valent substituted ferroelectric perovskites, Comput. Mater. Sci. 29 (2004) 67–75.

[16] I. Fujii, M. Ugorek, S Trolier-McKinstry, Grain size effect on the dielectric nonlinearity of $BaTiO_3$ ceramics, J. Appl. Phys. 107 (2010) 104116–104121.

[17] S. Fuentes, E. Chávez, L. Padilla-Campos, D.E. Diaz-Droguett, Ceram. Int., http://dx.doi.org/10.1016/j.bbr.2011.03.031.

[18] A.D. Becke, Density-functional thermochemistry. III. The role of exact exchange, J. Chem. Phys. 98 (1993) 5648–5653.

[19] A.D. Becke, Density-functional exchange-energy approximation with correct asymptotic behavior, Phys. Rev. A 38 (1988) 3098–3100.

[20] B. Miehlich, A. Savin, H. Stoll, H. Preuss, Results obtained with the correlation energy density functionals of Becke and Lee, Yang and Parr, Chem. Phys. Lett. 157 (1989) 200–206.

[21] C. Lee, W. Yang, G.R. Parr, Development of the Colle–Salvetti correlation-energy formula into a functional of the electron density, Phys. Rev. B 37 (1988) 785–789.

[22] W.J. Hehre, R. Ditchfield, J.A. Pople, Self-consistent molecular orbital methods. XII. Further extensions of Gaussian-type basis sets for use in molecular orbital studies of organic molecules, J. Chem. Phys. 56 (1972) 2257–2261.

[23] P.J. Hay, W.R. Wadt, Ab initio effective core potentials for molecular calculations. Potentials for the transition metal atoms Sc to Hg, J. Chem. Phys. 82 (1985) 270–284.

[24] S. Piskunov, E.A. Kotomin, D. Fuks, S. Dorfman, Ab initio calculations of the atomic and electronic structure of layered $Ba_{0.5}Sr_{0.5}TiO_3$ structures, Mater. Sci. Eng. B 118 (2005) 15–18.

[25] S.Y. Kuo, W.Y. Liao, W.F. Hsieh, Structural ordering transition and repulsion of the giant LO–TO splitting in polycrystalline $Ba_xSr_{1-x}TiO_3$, Phys. Rev. B 64 (2001) 224103–224110.

[26] E. Chávez, S. Fuentes, R. Zárate, L. Padilla-Campos, Structural analysis of nanocrystalline $BaTiO_3$, J. Mol. Struct. 984 (2010) 131–136.

[27] J. Cioslowski, A new population analysis based on atomic polar tensor, J. Am. Chem. Soc. 111 (1989) 8333–8336.

[28] M.J. Frisch, G.W. Trucks, H.B. Schlegel, G.E. Scuseria, M.A. Robb, J.R. Cheeseman, G. Scalmani, V. Barone, B. Mennucci, G.A. Petersson, H. Nakatsuji, M. Caricato, X. Li, H.P. Hratchian, A.F. Izmaylov, J. Bloino, G. Zheng, J.L. Sonnenberg, M. Hada, M. Ehara, K. Toyota, R. Fukuda, J. Hasegawa, M. Ishida, T. Nakajima, Y. Honda, O. Kitao, H. Nakai, T. Vreven, J.A. Montgomery Jr., J.E. Peralta, F. Ogliaro, M. Bearpark, J.J. Heyd, E. Brothers, K.N. Kudin, V.N. Staroverov, T. Keith, R. Kobayashi, J. Normand, K. Raghavachari, A. Rendell, J.C. Burant, S.S. Iyengar, J. Tomasi, M. Cossi, N. Rega, J.M. Millam, M. Klene, J.E. Knox, J.B. Cross, V. Bakken, C. Adamo, J. Jaramillo, R. Gomperts, R.E. Stratmann, O. Yazyev, A.J. Austin, R. Cammi, C. Pomelli, J.W. Ochterski, R.L. Martin, K. Morokuma, V. G. Zakrzewski, G.A. Voth, P. Salvador, J.J. Dannenberg, S. Dapprich, A.D. Daniels, O. Farkas, J.B. Foresman, J.V. Ortiz, J. Cioslowski, D. J. Fox, Gaussian 09, Revision B.01, Gaussian, Inc., Wallingford, CT, 2010.

[29] D. Tenne, X. Xi, Raman spectroscopy of ferroelectric thin films and superlattices, J. Am. Ceram. Soc. 91 (2008) 1820–1834.

[30] W.H. Zhang, L. Chen, Y.T. Tao, W.H. Zhang, J. Chen, J. Zhang, Raman study of barium titanate with oxygen vacancies, Physica B 406 (2011) 4630–4633.

[31] Y. Du, G. Chen, M. Zhang, Investigation of structural phase transition in polycrystalline $SrTiO_3$ thin films by Raman spectroscopy, Solid State Commun. 130 (2004) 577–580.

[32] W. Kleemann, A. Albertini, M. Kuss, R. Linder, Optical detection of symmetry breaking on a nanoscale in $SrTiO_3$:Ca, Ferroelectrics 203 (1997) 57–74.

[33] I. Akimov, A. Sirenko, A. Clark, J. Hao, X. Xi, Electric-field-induced soft-mode hardening in $SrTiO_3$ films, Phys. Rev. Lett. 84 (2000) 4625–4628.

[34] W.G. Nilsen, J.G. Skinner, Raman Spectrum of strontium titanate, J. Chem. Phys. 48 (1968) 2240–2249.

[35] J.I. Dos Santos, G.A. Barbosa, Disorder manifestation in the light scattering spectra of $SrTiO_3$ at high temperatures, Ferroelectrics 25 (1980) 625–627.

[36] F. Rabuffetti, H. Kim, J. Enterkin, Y. Wang, C. Lanier, L. Marks, K. Poppelmeier, P. Stair, Synthesis dependent first orden raman scattering in $SrTiO_3$ nanocubes at room temperature, Chem. Mater. 20 (2008) 5628–5635.

[37] D. Tenne, A. Soukiassian, X. Xi, H. Choosuwan, R. Guo, A. Bhalla, Lattice dynamics in $Ba_xSr_{1-x}TiO_3$ single crystals: a Raman study, Phys. Rev. B 70 (2004) 174302–174311.

[38] D. Ehre, H. Cohen, V. Lyahovitskaya, I. Lubomirsky, X-ray photoelectron spectroscopy of amorphous and quasiamorphous phases of $BaTiO_3$ and $SrTiO_3$, Phys. Rev. B 77 (2008) 184106–184112.

[39] C. Xu, Y. Xia, Z. Liu, X. Meng, Chemical states change at (Ba,Sr)TiO_3/Pt interfaces investigated by X-ray photoelectron spectroscopy, J. Phys. D: Appl. Phys. 42 (2009) 085302–085310.

[40] J.X Liao, C.R. Yang, Z. Tian, H.G. Yang, L. Jin, The influence of post-annealing on the chemical structures and dielectric properties of the surface layer of $Ba_{0.6}Sr_{0.4}TiO_3$ films, J. Phys. D: Appl. Phys. 39 (2006) 2473–2478.

[41] B. Zhang, Z. Quan, T. Zhang, T. Guo, S. Mo, Effect of oxygen gas and annealing treatment for magnetically enhanced reactive ion etched $(Ba_{0.65},Sr_{0.35})TiO_3$ thin films, J. Appl. Phys. 101 (2007) 014107–014115.

[42] Nasser, X-ray photoelectron spectroscopy study on the composition and structure of $BaTiO_3$ thin films deposited on silicon, Appl. Surf. Sci. 157 (2000) 14–22.

[43] T.A. Kaplan, S.D. Mahanti, Electronic Properties of Solids Using Cluster Methods, Plenum Press, New York, 1995.

[44] L. Padilla-Campos, P. Fuentealba, Theoretical study of the adsorption of oxygen on a Cu(100) surface and the coadsorption with alkali atoms, Theor. Chem. Acc. 110 (2003) 414–420.

[45] L. Padilla-Campos, A theoretical investigation of occupation sites for tritium atoms in lithium titanate, J. Mol. Struct. (Theochem.) 621 (2003) 107–112.